



LOFAR Deep Fields: Probing the sub-mJy regime of polarized extragalactic sources in ELAIS-N1 II. Analysis

Downloaded from: <https://research.chalmers.se>, 2025-01-20 16:02 UTC

Citation for the original published paper (version of record):

Piras, S., Horellou, C., Conway, J. et al (2025). LOFAR Deep Fields: Probing the sub-mJy regime of polarized extragalactic sources in ELAIS-N1 II. Analysis. *Astronomy and Astrophysics*, 693. <http://dx.doi.org/10.1051/0004-6361/202451039>

N.B. When citing this work, cite the original published paper.

LOFAR Deep Fields: Probing the sub-mJy regime of polarized extragalactic sources in ELAIS-N1

II. Analysis

S. Piras^{1,*}, C. Horellou², J. E. Conway², M. Thomasson¹, T. W. Shimwell^{3,4}, S. P. O’Sullivan⁵,
 E. Carretti⁶, V. Vacca⁷, A. Bonafede^{6,8}, and I. Prandoni⁶

¹ Department of Space, Earth and Environment, Chalmers University of Technology, 412 96 Gothenburg, Sweden

² Department of Space, Earth and Environment, Chalmers University of Technology, Onsala Space Observatory, 43992 Onsala, Sweden

³ ASTRON, Netherlands Institute for Radio Astronomy, Oude Hoogeveensedijk 4, 7991 PD Dwingeloo, The Netherlands

⁴ Leiden Observatory, Leiden University, PO Box 9513, 2300 RA Leiden, The Netherlands

⁵ Departamento de Física de la Tierra y Astrofísica & IPARCOS-UCM, Universidad Complutense de Madrid, 28040 Madrid, Spain

⁶ INAF Istituto di Radioastronomia, Via Gobetti 101, 40129 Bologna, Italy

⁷ INAF-Osservatorio Astronomico di Cagliari, Via della Scienza 5, 09047 Selargius (CA), Italy

⁸ DIFA Università di Bologna, via Gobetti 93/2, 40129 Bologna, Italy

Received 8 June 2024 / Accepted 30 October 2024

ABSTRACT

Context. Deep polarization surveys at low radio frequencies are key to cosmic magnetism studies: Larger catalogs of polarized extragalactic sources and increased precision on Faraday rotation measures (RMs) make it possible to probe the magneto-ionic medium along the lines of sight of the sources and to construct denser RM grids. In a first paper, we presented a search for polarized sources in deep observations of the 25-square-degree area of the European Large Area ISO Survey-North 1 (ELAIS-N1) field with the LOw Frequency ARray (LOFAR) at 114.9–177.4 MHz.

Aims. In this paper, we investigate the properties of the polarized radio galaxies and use the catalog to produce an RM grid of the field.

Methods. After identifying the host galaxies and collecting redshift information, we characterized the radio galaxies in terms of their radio morphologies, rest-frame radio luminosities, and linear sizes. We calculated residual rotation measures (RRMs) by removing the Galactic RM and studied the variation in the RRM with redshift and degree of polarization. We produced an RRM grid of the field and compared the positions of the polarized sources with those of galaxy clusters and superclusters.

Results. The radio galaxies show a variety of morphologies, including diffuse emission; Fanaroff Riley type II sources make up about half of the sample. Using available multiband catalogs, we found redshifts for the hosts of all polarized sources in the range of 0.06–1.9. Polarized emission is detected mainly from large radio galaxies. The RRM values have a median close to zero, and they appear to be independent of redshift and degree of polarization. The sources in the lines of sight of clusters of galaxies and of a supercluster are indistinguishable in their polarization and RRM properties from the population of sources that are not behind these structures.

Key words. polarization – methods: data analysis – methods: observational – galaxies: individual: ELAIS-N1

1. Introduction

Observations of polarized synchrotron radiation at radio frequencies are the most direct probes of cosmic magnetism. As radiation from an extragalactic source traverses a magneto-ionic medium, its plane of polarization experiences Faraday rotation, an effect that is proportional to the square of the wavelength of the EM wave. The observed rotation measure (RM; expressed in rad m^{-2}), is related to the product of the thermal electron density, n_e , and the line-of-sight component of the magnetic field, B_{\parallel} , integrated along the line of sight,

$$\left(\frac{\text{RM}}{\text{rad m}^{-2}} \right) = 0.812 \int_{\ell=0}^{\ell=L} \left(\frac{n_e(\ell)}{\text{cm}^{-3}} \right) \left(\frac{B_{\parallel}(\ell)}{\mu\text{G}} \right) \left(\frac{d\ell}{\text{pc}} \right). \quad (1)$$

The observed RM depends on all the contributing magneto-ionic media between the source and the observer, including the Galactic interstellar medium, the intergalactic medium, intervening galaxies, and the plasma within the source itself. So-called RM grids (i.e., collections of RM values across the sky) are a potentially powerful tool for investigating magnetic fields. To distinguish the different contributions to the RMs, it is crucial to identify the optical and/or IR counterparts to the polarized radio sources, however, and to obtain redshift information on the host galaxies to characterize the sources that constitute the RM grid in terms of their radio morphologies, their sizes, and other properties.

Traditionally, RM grid studies were conducted at 1.4 GHz and were hampered by large systematic uncertainties because the frequency sampling was poor. The largest RM catalog available to date is that of Taylor et al. (2009), which was produced from

* Corresponding author; sara.piras@chalmers.se

Table 1. Properties of the LoTSS-DR2 RM catalog and of the ELAIS-N1 LOFAR Deep Field catalog.

Catalog	Reference	Area (deg ²)	Resolution (arcsec)	ν_c (MHz)	$\Delta\nu$ (MHz)	$\delta\phi$ (rad m ⁻²)	σ_{QU} (μ Jy beam ⁻¹)	N_{RM}	N_{RG}	N_z
LoTSS-DR2 RM	(1)	5720	20	144	48	1.16	75	2461	1980	1783
ELAIS-N1	(2)	25	6	146	63	0.9	20	33	31	31

Notes. (1) O’Sullivan et al. (2023). The quoted σ_{QU} noise value corresponds to the median detection threshold, $8\sigma_{QU} = 0.6$ mJy beam⁻¹. (2) Paper I. The quoted noise value is the value measured at the center of the ELAIS-N1 field. ν_c is the central frequency, $\Delta\nu$ is the bandwidth, $\delta\phi$ is the resolution of the Faraday spectra, and σ_{QU} is the noise level in the Stokes Q and U Faraday cubes (Paper I). N_{RM} is the number of entries in the RM catalogs. N_{RG} is the number of radio galaxies associated with at least one RM value. N_z is the number of radio galaxies with a known redshift and associated with at least one RM value.

the National Radio Astronomy Observatory (NRAO) Very Large Array (VLA) Sky Survey (NVSS; Condon et al. 1998). The catalog contains RM values for 37 543 lines of sight to polarized radio sources and covers the sky north of a declination -40° at a resolution of 45 arcsec (82% of the whole sky). Through cross-matching with redshift catalogs, Hammond et al. (2012) identified a total of 4003 matches for the NVSS RM catalog. More recently, a new generation of telescopes operating at lower frequencies has been used to map the sky and obtain more precise RM values through low-frequency broadband polarimetry. In particular, at the LOFAR Two-Metre Sky Survey (LoTSS; Shimwell et al. 2017, 2019) provided data at 144 MHz with a resolution of 20 arcsec that were used to produce the LoTSS-DR2 RM catalog (O’Sullivan et al. 2023), a collection of ~ 2500 high-precision (~ 1 rad m⁻²) RM values from extragalactic polarized sources over 5720 deg² of the northern sky (Table 1). The catalog also contains host galaxy identifications for 88% of the sources, along with redshifts for 79%.

Observations at different wavelengths and of sources at different redshifts are required to distinguish the different RM contributions. Vernstrom et al. (2019) studied differences in RMs between adjacent NVSS sources on the sky (1.4 GHz; Condon et al. 1998; Taylor et al. 2009) and concluded that these variations may indicate the detection of an extragalactic RM signal. O’Sullivan et al. (2020) applied the method of Vernstrom et al. (2019) to the LoTSS (144 MHz, Shimwell et al. 2019) and placed an upper limit of 4 nG on the cosmological comoving magnetic field strength on megaparsec (Mpc) scales. Carretti et al. (2022) compared data from the NVSS and LoTSS-DR2 RM catalogs and found that the observed residual RM (RRM; obtained after subtraction of the Galactic RM) is most likely to have an origin local to the source at 1.4 GHz, while a cosmic web filament origin is favored at 144 MHz. This shows that RM studies at low radio frequencies have important implications on our understanding of the processes related to magnetic fields in the Universe (Carretti et al. 2023).

Depolarization is the primary challenge in low-frequency polarization studies (e.g., Stuardi et al. 2020, Mahatma et al. 2021), hence the need for deep polarization surveys. The ELAIS-N1 LOFAR Deep Field (Sabater et al. 2021) is best suited for a deep search for polarization. Herrera Ruiz et al. (2021) stacked LOFAR polarization datasets from observations of this field that were carried out at six epochs. They reached a 1σ sensitivity of 26 μ Jy beam⁻¹ in the final Stokes Q and U images at a resolution of 20'' and detected ten polarized sources in an area of 16 deg².

In Piras et al. (2024) (hereafter Paper I), we developed a new method to stack LOFAR datasets that were taken in different observing cycles with different frequency configurations, and we applied the method to the ELAIS-N1 LOFAR Deep Field to produce the most sensitive polarization dataset at 150 MHz so

far. Stacking polarization datasets from 19 epochs, we reached the lowest noise level of $\sigma_{QU} \sim 20$ μ Jy beam⁻¹ in the central region of the final 25 deg² image of the ELAIS-N1 field at a resolution of 6 arcsec (the deep Stokes I image of Sabater et al. 2021 was produced by combining data from 22 epochs, or an effective observing time of 163.7 hours, and had a similar noise level). We compiled a catalog of 31 polarized radio galaxies, 25 of which were identified through a systematic search across the entire field (setting a threshold for the signal-to-noise ratio of 8), while the remaining sources were identified through a study of the sources known to be polarized at 1.4 GHz from the works of Grant et al. (2010) and Taylor et al. (2009). For these sources, we lowered our detection threshold to $6\sigma_{QU}$. We derived the polarized source counts and modeled them based on the total flux density counts obtained by Mandal et al. (2021) in their study of three LOFAR Deep Fields that included ELAIS-N1. Some properties of the ELAIS-N1 LOFAR Deep Field RM catalog and of the LoTSS-DR2 RM catalog are summarized in Table 1.

The ELAIS-N1 LOFAR Deep Field (Sabater et al. 2021) has rich multiwavelength ancillary data that cover a broad range of the electromagnetic spectrum from X-ray to radio bands in its central region (inner 7.15 deg²). Through this wealth of information, the host galaxies of radio sources could be identified (Kondapally et al. 2021), and photometric redshifts were derived whenever spectroscopic redshifts were not available (Duncan et al. 2021). With its exceptional depth and image quality, the ELAIS-N1 LOFAR Deep Field presents an optimal setting for diverse scientific investigations, such as the search for diffuse emission within clusters of galaxies (Osinga et al. 2021), the examination of an alignment in radio galaxies (Simonte et al. 2023), the search for giant radio galaxies (Simonte et al. 2024), and studies of the spectral properties of star-forming galaxies (An et al. 2024) and of the Galactic polarized emission (Šnidarić et al. 2023).

In this paper, we exploit the ELAIS-N1 multiband information to characterize the extragalactic polarized sources presented in Paper I and compare their properties with those of the LoTSS-DR2 RM catalog (Sect. 2). Because LOFAR data lack an absolute polarization calibration, we present no relation between the intrinsic (zero-wavelength) polarization angles and the source major-axis position angles, for example; only the rotation of the polarization angles with frequency can be measured. In Sect. 3 we present an analysis of the RM and RRM grids of the ELAIS-N1 LOFAR Deep Field, and we conclude in Sect. 4.

In the calculations of the rest-frame luminosities and projected linear sizes of the radio galaxies from which polarization was detected, we used the following values of cosmological parameters for a flat Λ cold dark matter model: $H_0 = 67.8$ km s⁻¹ Mpc⁻¹ and $\Omega_m = 0.308$ (Planck Collaboration XIII 2016).

Table 2. Radio morphological classification and some properties of the polarized radio galaxies in the ELAIS-N1 LOFAR Deep Field.

Type	<i>N</i>	Fraction	ID of polarized component in Paper I
Compact	4	$12.9 \pm 6.5\%$	09, 10, 24, 25
FRI	4	$12.9 \pm 6.5\%$	06, 14, 18, 32
FR II	18	$58.1 \pm 13.7\%$	01, 02, 04 _A + 04 _B ; 05, 07, 08, 11, 12; 13 _A ^(a) + 29; 15, 17, 19, 21, 23, 26, 27 ^(b) , 30, 31 ^(b)
Other Extended	5	$16.1 \pm 7.2\%$	03, 16, 20 ^(c) , 22, 28
Total	31	100%	
Radio size > 500 kpc	9	$29.0 \pm 9.7\%$	08, 11, 12; 13 _A + 29; 15, 18, 23, 26, 32
Radio size > 1 Mpc	3	$9.7 \pm 5.6\%$	11, 12, 23

Notes. *N* is the number of radio galaxies. The uncertainties associated with the fractional number of sources of a given type are Poissonian ($\sqrt{N}/31$). a) Sources 13_A and 29 (13_B) are two lobes of the same FR II radio galaxy. b) Source 27 and 31 were classified as FRIs by Mingo et al. (2022), but after visual inspection, we classified them as FR IIs. c) Source 20 appears to be a one-sided blazar.

2. Properties of the detected polarized sources

In this section, we examine some key properties of the radio galaxies in ELAIS-N1 for which polarization was reported in Paper I: radio morphology, redshift of their hosts, projected linear size, and rest-frame luminosity. These properties are compared with those of the radio galaxies in the LoTSS-DR2 RM catalog of O’Sullivan et al. (2023).

2.1. Radio morphology

In Appendix B (available on Zenodo¹) we show the 6'' resolution LOFAR Stokes *I* images of the sources in which polarization was detected and the corresponding Faraday spectra at the pixel of the peak polarized intensity. The images were extracted from the large Stokes *I* image of Sabater et al. (2021). The pixels in blue are the positions at which polarized intensity was detected in the range indicated by the color scale. The polarized emission is unresolved in all the detected sources. A description of each source is given in Appendix C.

The radio sources present a variety of morphologies that we classified into four categories: compact, Fanaroff–Riley types I and II (FRI and FR II; Fanaroff & Riley 1974), and other extended sources. FRI radio galaxies are center-brightened and become fainter toward the outer extremities of the lobes, FR II radio galaxies are edge-brightened and generally terminate in hotspots, sources classified as compact are those whose full width at half maximum (FWHM) of the deconvolved major axis is smaller than or equal to 6'' in the Sabater et al. (2021) catalog, and the other extended sources are those whose deconvolved FWHM is greater than 6'', which cannot be classified as FRI or FR II galaxies.

In the central region of the ELAIS-N1 LOFAR Deep Field with rich multiwavelength information (shown in Fig. 1 of Paper I), we detected polarization from 18 radio galaxies; 10 of them are listed as FRI or FR II in the catalog of Mingo et al. (2022)². We classified the remaining sources in the field

through visual inspections of the LOFAR Stokes *I* image with a resolution of 6 arcsec of Sabater et al. (2021) and of images from the Very Large Array Sky Survey (VLASS). We also inspected images of the 10 polarized sources in our sample that were morphologically classified by Mingo et al. (2022), and we reclassified two of them, as indicated in the footnote of Table 2.

In Table 2 we present the result of the classification of the radio galaxies from which we detected polarization. About half of the sources are classified as FR II radio galaxies, and the other half are about equally distributed among the other classes (four to six sources in each category).

The fraction of polarized radio sources that are classified as FRI galaxies is lower in the ELAIS-N1 LOFAR Deep Field (~13%) than in the LoTSS-DR2 RM sample (~20%). The fraction of detected polarized FR IIs is higher in ELAIS-N1 (~58%) than in LoTSS-DR2 RMs (~40%). However, this difference may not be significant when Poissonian errors are taken into account ($\sim 58 \pm 14\%$ in ELAIS-N1) and considering that approximately 15% of the LoTSS-DR2 RM sources were classified as hybrid when their FR category could not be reliably assessed.

We also examined the fraction of FRI or FR II radio galaxies from which we detected polarization in the multiwavelength part of the field studied by Mingo et al. (2022), who identified 160 FRI and 126 FR II radio galaxies in total intensity (with angular sizes greater than 27'' and at $z < 2.5$). As mentioned above, some of the sources may be classified differently after a detailed visual inspection. The fact that we detected polarization from more FR II than FRI radio galaxies in the multiwavelength region in which Mingo et al. (2022) found more FRI radio galaxies is an indication that the detection rate of polarization from FR II radio galaxies is higher than that from FR Is.

In ELAIS-N1, polarization from FR II radio galaxies is detected in lobes or hotspots that are located at large projected distances from their host galaxies, and in FR Is, polarization is found in the more central regions, likely from inner jets (this might be a selection effect, however). The larger fraction of detected polarized FR IIs might indicate different depolarizing environments through which the polarized emission travels. The lobes of FR IIs may expand in lower-density ionized environments, which are characterized by weaker magnetic fields that cause less depolarization (e.g., O’Sullivan et al. 2020; Stuardi et al. 2020; Carretti et al. 2022). The central regions of FR Is, in contrast, may be in denser magneto-ionic environments and are therefore more strongly affected by depolarization.

¹ <https://zenodo.org/records/14012234>

² Mingo et al. (2022) used the LoMorph Python code <https://github.com/bmingo/LoMorph> of Mingo et al. (2019) to classify FRI and FR II radio galaxies in the multiwavelength region of ELAIS-N1. Ten radio galaxies of the Mingo et al. (2022) sample are associated with our polarized components 08, 11; 13_A and 13_B; 18, 19, 20, 26, 27, 29 (= 13_B), 31, and 32.

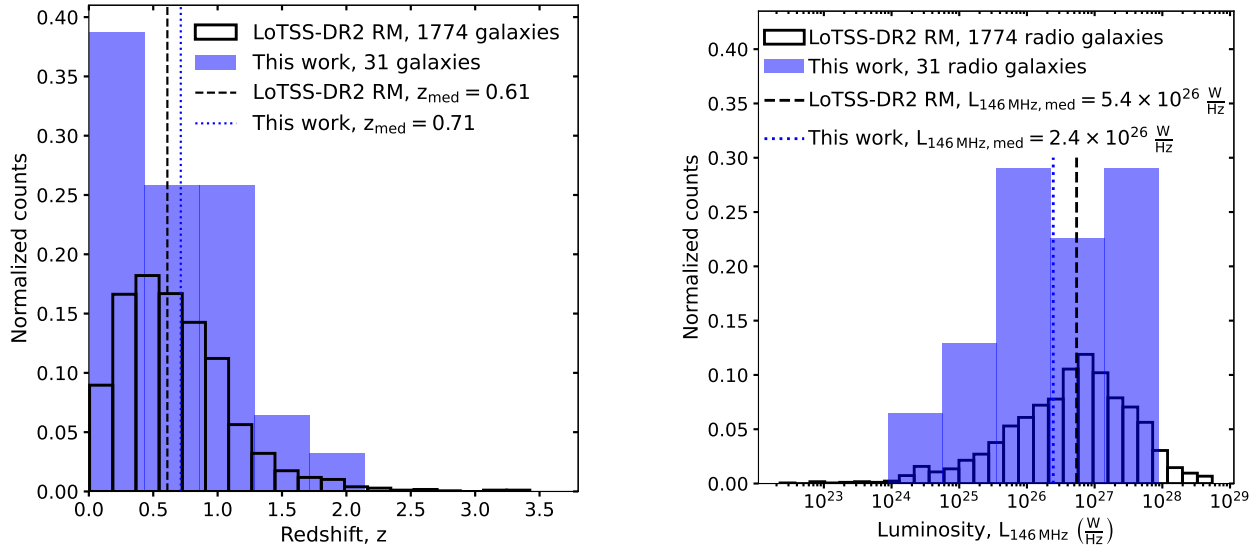


Fig. 1. Comparison of some properties of the ELAIS-N1 sample (this work) and the LoTSS-DR2 RM sample. *Left panel:* redshift distribution of the host galaxies of the radio galaxies in ELAIS-N1 in which we detected polarization (blue) and of the radio galaxies in the LoTSS-DR2 RM sample (black). *Right panel:* distribution of rest-frame luminosities for our catalog (blue) and for the LoTSS-DR2 RM catalog computed at 146 MHz (black). The median values are indicated by vertical lines and given in Table 3.

Herrera Ruiz et al. (2021) detected polarization in ten radio galaxies, including three compact ones, three FRIs, and three FRII. The authors did not assign any morphological class to their source 2 (our source 7, which we classify as an FRII). In the LoTSS Preliminary Data Release (at the low resolution of $4.3''$), Van Eck et al. (2018) found only one FRI radio galaxy out of 92 polarized sources, which led Herrera Ruiz et al. (2021) to suggest that deeper observations could enhance the detection rate of polarized emission from the extended regions of FRI radio galaxies. However, after stacking 19 epochs and considering Poissonian errors, our fraction of polarized FRI radio galaxies ($\sim 13\%$) is lower than that of Herrera Ruiz et al. (2021) (who reported 30%). In all the FRIs that we detected, polarization was found in the core and not in the lobes.

2.2. Host galaxies and redshifts

Table A.1 lists 33 entries that correspond to polarized components associated with 31 radio galaxies (source 4 has two polarized components, 04_A and 04_B, and components 13_A and 29 (13_B) belong to the same radio galaxy). As described in more detail below, we were able to obtain redshift estimates from the literature for all radio galaxies in the sample (26 spectroscopic and 5 photometric).

For about half of our sample, host galaxies and redshifts were reported by Simonte et al. (2024) in their investigation of extended radio galaxies in the three LOFAR Deep Fields (which included the 25 deg² area of ELAIS-N1). A cross-match of our catalog with theirs provided a host identification and redshift for 16 radio galaxies (associated with our polarized components 4, 5, 6, 8, 11, 12, 13, 14, 16, 17, 18, 19, 22, 27, 31, and 32). For the remaining sources, we associated the host galaxy and the redshift from the catalog from the 16th data release from the Sloan Digital Sky Survey (SDSS) by Ahumada et al. (2020), using the images from the Dark Energy Spectroscopic Instrument (DESI) Legacy Imaging Surveys³ (DESI Collaboration 2024) and the NASA/IPAC Extragalactic Database (NED⁴).

³ <https://www.legacysurvey.org/>

⁴ <https://ned.ipac.caltech.edu/>

In Fig. 1 (left panel) we show the redshift distributions of the host galaxies of radio galaxies with at least one polarized component in ELAIS-N1 and of those in the LoTSS-DR2 RM catalog. The median redshift is higher for the ELAIS-N1 catalog than for the LoTSS-DR2 RM sample, as indicated in the legend.

2.3. Rest-frame spectral luminosities

The central frequency of the LOFAR observations of the ELAIS-N1 Deep Field is 146 MHz, and that of LoTSS-DR2 is 144 MHz. For the radio galaxies in our ELAIS-N1 catalog, we calculated the rest-frame spectral luminosities at 146 MHz following the equation (Condon & Matthews 2018)

$$L_{146 \text{ MHz}} = S_{146 \text{ MHz}} \frac{4\pi D_L^2(z)}{(1+z)^{1+\alpha}}, \quad (2)$$

where $S_{146 \text{ MHz}}$ is the flux density of the source, D_L is the luminosity distance, and $\alpha = -0.7$ is the spectral index ($S \propto \nu^\alpha$). In LoTSS-DR2, rest-frame luminosities at 144 MHz were derived using the same values of the cosmological parameters and assuming the same spectral index value. To compare the two samples, we scaled the published LoTSS-DR2 144 MHz rest-frame luminosities down by a factor of $(146/144)^{-0.7} \sim 0.99$ to obtain the rest-frame luminosities at 146 MHz.

In ELAIS-N1, we estimated the flux densities of the sources from the Stokes I image of Sabater et al. (2021) using Martin Hardcastle's code `radioflux`⁵, which sums the intensities within a selected area of the image. For the sources in common with the catalog of Simonte et al. (2024) (the radio galaxies associated with our polarized components 11, 12, 13, 15, 23, and 26), we used the values provided by those authors who measured the flux densities more carefully for these extended sources.

In Fig. 1 we show the distributions of 146 MHz rest-frame luminosities for the two samples. The median quantities are given in Table 3. In ELAIS-N1 we detect polarization from radio sources that are fainter on average than those in the LoTSS-DR2 RM catalog (we scaled the 144 MHz flux densities from

⁵ <https://github.com/mhardcastle/radioflux>

Table 3. Median quantities of the ELAIS-N1 sample and of the LoTSS-DR2 RM sample of radio galaxies with a known redshift and at least one polarized component: redshift, flux density at 146 MHz, rest-frame 146 MHz spectral luminosity, or number of sources in each sample.

	z	$S_{146 \text{ MHz}}$ (mJy)	$L_{146 \text{ MHz}}$ (W Hz ⁻¹)	N
This work	0.71	190	2.4×10^{26}	31
LoTSS-DR2 RM	0.61	403	5.4×10^{26}	1774

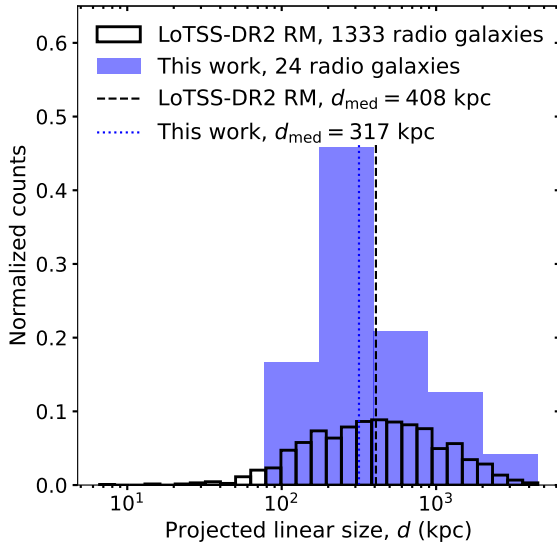


Fig. 2. Distribution of the projected linear sizes of the subset of resolved radio galaxies in both catalogs. The median values are indicated.

the LoTSS-DR2 RM catalog by the factor mentioned above before we calculated the median at 146 MHz). The population of polarized sources in ELAIS-N1 is at a higher median redshift than the polarized sources in LoTSS-DR2 RM catalog, and the median rest-frame luminosity is lower in ELAIS-N1. This was to be expected from deeper observations: We are able to detect some fainter sources that are more distant and/or intrinsically less luminous. As expected from the lower median rest-frame luminosity in ELAIS-N1, the fraction of sources above the traditional FRI/FRII luminosity separation of $\sim 10^{26}$ W Hz⁻¹ is lower in ELAIS-N1 ($\sim 60\%$ of the sources) than in the LoTSS-DR2 RM catalog (about 66%).

2.4. Linear sizes

In Fig. 2 we show the distribution of projected linear sizes of resolved radio galaxies associated with at least one polarized component in ELAIS-N1 and in the LoTSS-DR2 RM catalog. Radio galaxies in our samples are classified as resolved when their angular size is greater than $15''$ (and as unresolved otherwise). This criterion is similar to the one used by (Shimwell et al. 2022) and adopted for the LoTSS-DR2 RM catalog. In Table A.1 we list the sizes (both the angular sizes and the projected linear sizes on the sky) of the radio galaxies in our sample. The projected linear sizes are always lower limits to the true sizes in three-dimensional space of the radio galaxies.

For 23 of the radio galaxies in which we detected polarization⁶, we took the values of the angular sizes provided by Simonte et al. (2024). For 6 radio galaxies⁷, we took the values from Sabater et al. (2021). For 2 radio galaxies (sources 1 and 7), we determined the angular sizes by inspecting the total-intensity image of Sabater et al. (2021); this was necessary as these sources are FRII radio galaxies but were not resolved into two components in the catalog of Sabater et al. (2021).

In the LoTSS-DR2 RM catalog, the majority of the radio galaxies in which polarization was found are large radio galaxies with a median projected size of ~ 408 kpc for the resolved sources and ~ 300 kpc (including upper limits) for the unresolved sources. The median projected linear size of our resolved radio galaxies is ~ 317 kpc, and it is ~ 235 kpc for the entire sample (including upper limits for the unresolved radio galaxies), suggesting that the radio galaxies in ELAIS-N1 in which we detect polarization with LOFAR are also mainly large radio galaxies. We find nine sources with a projected linear size greater than 500 kpc (Table 2); three of these are giant radio galaxies (sources 11, 12, and 23) with sizes greater than 1 Mpc.

In Fig. 3 (left panel) we show the degree of polarization of the polarized component as a function of the projected linear size for the radio galaxies in which we detected polarization and for the LoTSS-DR2 RM sample. In both catalogs, the fractional polarization was computed at the pixel of the detection of polarization in the polarized intensity map and at the corresponding pixel in the total-intensity map.

In the LoTSS-DR2 RM catalog the degree of polarization increases with projected linear size. In ELAIS-N1 we considered the resolved radio galaxies and divided the sample into two bins of linear sizes, with equal numbers of components in each bin. We found a median degree of polarization of 2.2% for sizes in the 91–315 kpc range and of 4.1% in the 315 kpc–2.1 Mpc size range. While our findings are consistent with the increase in the degree of polarization observed in the LoTSS-DR2 RM catalog, they are limited by the small size of our sample (24 radio galaxies, 12 per bin).

In Fig. 3 (right panel) we show the degree of polarization of the polarized component as a function of projected distance from the center of the host galaxy to the polarized component for the 33 polarized components of the ELAIS-N1 LOFAR Deep Field and for the 1948 polarized components associated with host galaxies with a known redshift in the LoTSS-DR2 RM catalog. At projected distances from the host of $d > 100$ kpc, the degree of polarization of the polarized component increases with increasing distance from the host galaxy. At these projected distances, the polarized components are likely to be exclusively distant hotspots of FRII radio galaxies that are intrinsically strongly polarized; the fractional polarization continues to increase with distance from the host because the effect of the environment is weaker: Giant radio galaxies mostly reach large sizes because they expand in low-density environments; when the environment is sparser, the radio galaxy can become larger, and the distant hotspots/lobes are not as strongly depolarized.

3. LOFAR RM and RRM grid of ELAIS-N1

The extragalactic RM, called residual rotation measure (RRM), is obtained by subtracting the foreground Galactic RM (GRM)

⁶ Those containing the polarized sources 02, 04, 05, 06, 08, 11, 12, 13, 14, 15, 16, 17, 18, 19, 20, 21, 22, 23, 26, 27, 30, 31, and 32.

⁷ Polarized sources 03, 09, 10, 24, 25, and 28.

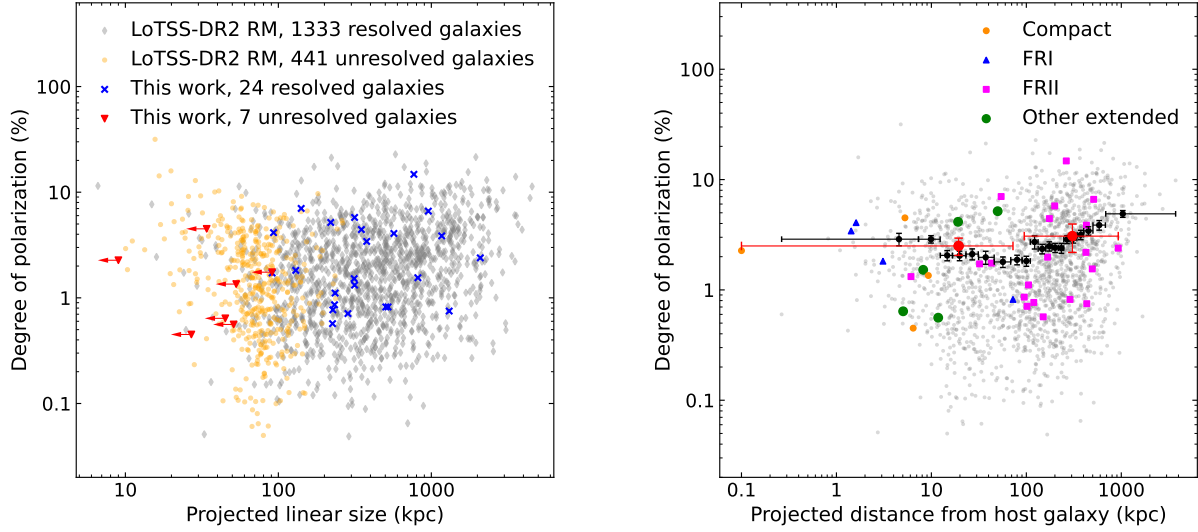


Fig. 3. Comparison of the variations of the degrees of polarization with linear size and with projected distance from the host in the ELAIS-N1 sample (this work) and in the LoTSS-DR2 RM sample. *Left panel:* degree of polarization of the polarized component as a function of the projected linear source size for the radio galaxies in the LoTSS-DR2 RM sample and for those of our ELAIS-N1 sample, with upper limits on the linear source sizes for unresolved radio galaxies (shown in orange for the LoTSS-DR2 RM sample and in red with horizontal arrows for the ELAIS-N1 sample). *Right panel:* degree of polarization of the polarized component as a function of the projected distance from the center of the host galaxy to the polarized component. The gray dots show the LoTSS-DR2 RM sample, and the other symbols represent different classes of radio galaxies in ELAIS-N1 in which polarization was detected. The black dots show the mean values in bins of 100 values for LoTSS-DR2-RM, and the red dots are the values for ELAIS-N1, where two bins of approximately equal numbers of polarized components were used. The horizontal lines show the width of each bin, and the vertical lines show the standard errors on the mean values.

from the observed RM,

$$\text{RRM} = \text{RM} - \text{GRM}. \quad (3)$$

To obtain the GRM values, we used the reconstruction of the Galactic Faraday depth sky of [Hutschenreuter et al. \(2022\)](#) and calculated the GRM as the average value within a circle with a diameter of one degree centered at the position of each RM source, as this is the typical separation between sources in the study by [Hutschenreuter et al. \(2022\)](#) (a similar approach was used by [Carretti et al. 2022](#) and [O’Sullivan et al. 2023](#)). The uncertainties associated with the RRM values were computed as $\sigma_{\text{RRM}} = \sqrt{\sigma_{\text{RM}}^2 + \sigma_{\text{GRM}}^2}$, where σ_{GRM} is the mean value of the GRM uncertainty map from [Hutschenreuter et al. \(2022\)](#) within the circle with a diameter of one degree. The RM, GRM, and RRM values are reported in Table A.1.

In Fig. 4 we show histograms of the RM, GRM, and RRM distributions. Because of instrumental polarization due to leakage from Stokes I into Stokes Q and U (Sect. 3.4 of Paper I), there is a gap in the RM distribution around zero that is absent in the RRM distribution that is obtained after the Galactic RM values were subtracted. The GRM values estimated from the map of [Hutschenreuter et al. \(2022\)](#) are mostly positive in the ELAIS-N1 field, with a mean value of about 6 rad m^{-2} , and a scatter that is smaller than that in the RM distribution. The RRM distribution obtained after the GRM values were subtracted is narrower than the RM distribution. The mean and the median RRM values are consistent with zero, as expected for a population of extragalactic sources whose polarized emission crosses the intergalactic magneto-ionic medium with random fluctuations of the electron-density-weighted parallel component of the magnetic field around zero. This was also reported in the LoTSS-DR2 RM studies of [Carretti et al. \(2022\)](#) and [O’Sullivan et al. \(2023\)](#).

Some statistical values are given in Table 4. In addition to the means and medians (and the dispersions around their values),

Table 4. Basic statistical properties of the RM and RRM distributions, all in rad m^{-2} , of the 33 polarized components in the ELAIS-N1 LOFAR Deep Field.

	Mean	std ^(a)	Median	MAD ^(b)	Mean(abs) ^(c)	rms ^(d)
RM	4.21	9.56	3.29	7.30	8.48	10.44
GRM	6.13	4.09	5.74	3.32	6.37	7.37
RRM	-1.92	6.77	-1.78	4.51	5.45	7.03

Notes. ^(a)Standard deviation. The quoted values use the default of the `numpy.std` Python command, which uses a normalization by N rather than by $N - 1$. ^(b)Median absolute deviation. ^(c)Mean of the absolute values. ^(d)Root mean square.

we list in the two last columns two indicators of the strengths of the various contributions: the mean of the absolute values, $\langle X \rangle$, and the root mean square (rms), $\langle X^2 \rangle^{1/2}$, where X is one of the RM-related variables (RM, GRM, or RRM). The rms is the most physically meaningful indicator because its square is related to the power ($\propto B_{\parallel}^2$) that is contained in the line-of-sight component of the magnetic field. The Galactic RM and the extragalactic RM (estimated by RRM) have comparable contributions, as estimated from their rms values ($\sim 7 \text{ rad m}^{-2}$).

In their reconstruction of the GRM sky, [Hutschenreuter et al. \(2022\)](#) used a number of RM catalogs, the largest of which were the NVSS RM catalog of [Taylor et al. \(2009\)](#) and the LoTSS-DR2 RM catalog of [O’Sullivan et al. \(2023\)](#). In the 25 deg^2 ELAIS-N1 LOFAR Deep Field, the NVSS catalog has 27 RM entries (2 of which are associated with sources that lie very close to the northern border of the field and were not included in the accounting presented in Table 1 of Paper I); the LoTSS-DR2 RM catalog has 9 entries (8 of these polarized sources are in our catalog; the ninth source is in the outskirts of our LOFAR pointing and was detected in LoTSS-DR2 RM because of the better

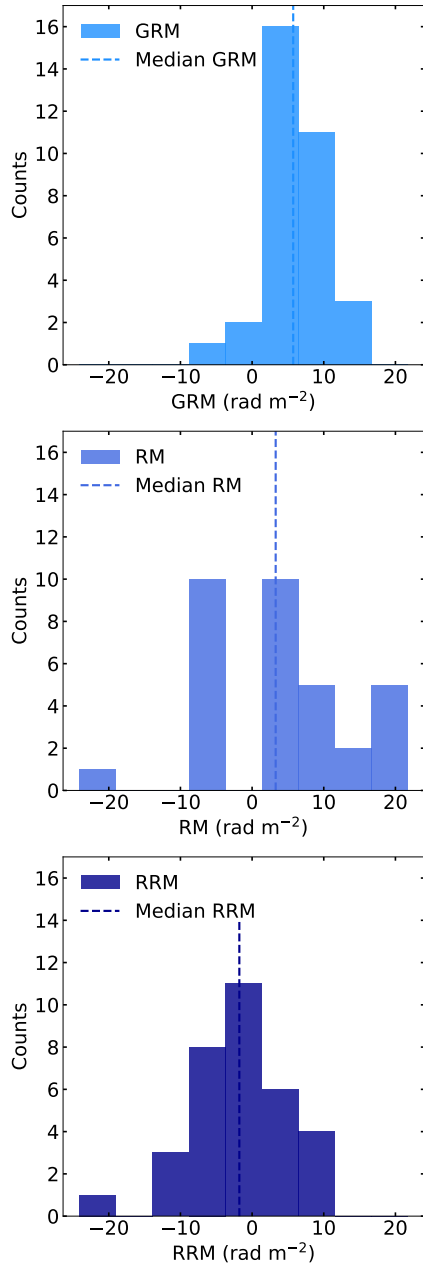


Fig. 4. Histograms of the GRM, RM, and RRM distributions for the 33 polarized components in the ELAIS-N1 LOFAR Deep Field.

signal-to-noise ratio that was gained by the mosaicking of two pointings at this location).

In Fig. 5 (first panel) we show the GRM map of the 25 deg² field of ELAIS-N1 extracted from the all-sky Galactic RM map of [Hutschenreuter et al. \(2022\)](#). The clear gradient across the field is also visible in the polarized foreground imaged with LOFAR at a resolution of 4.3' by [Šnidarić et al. \(2023\)](#). The other panels show the RM grid and the RRM grid obtained after subtraction of the GRM values. While the polarized foregrounds may originate in nearby Galactic structures and probably do not probe the full line of sight through the Milky Way, the similarity between the two maps is an indicator that the Galactic RM map of [Hutschenreuter et al. \(2022\)](#) is a reasonable estimate of the GRM. However, the fact that the gradient seen in the GRM map remains in the RRM grid might be a sign of a residual GRM contamination.

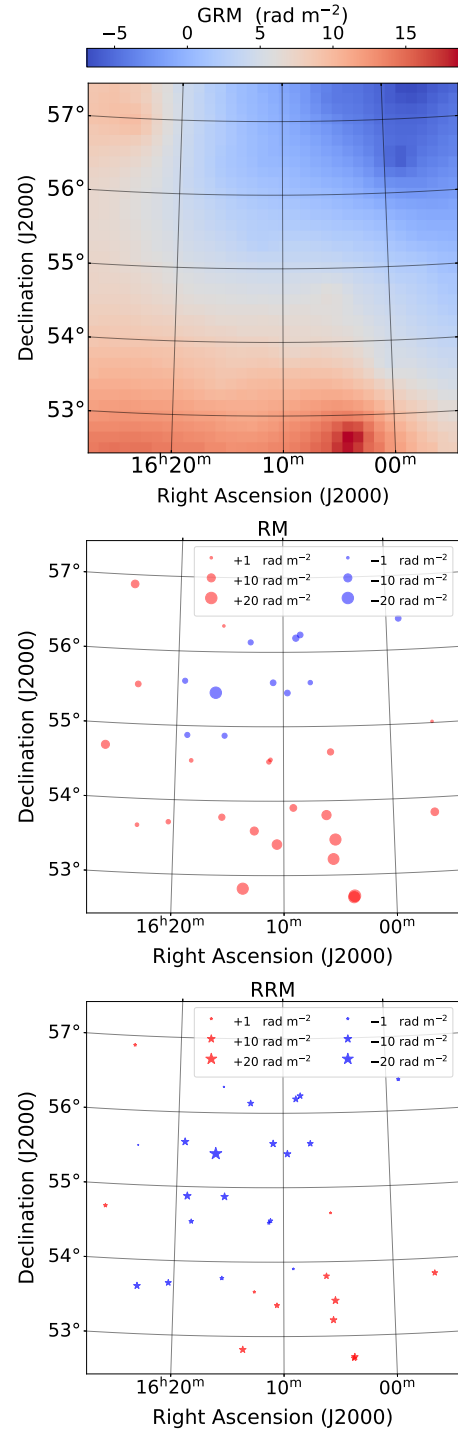


Fig. 5. Images of the GRM, RM, and RRM values. *Top panel:* Galactic RM map from [Hutschenreuter et al. \(2022\)](#). *Other panels:* distribution of polarized sources in the ELAIS-N1 LOFAR Deep Field. The size of the markers is proportional to the magnitude of the RM values (*middle panel*) and RRM values (*bottom panel*).

3.1. Redshift dependence of the RRM and fractional polarization

We examined the behaviors of the degree of polarization and of the absolute values of RRM, |RRM|, as a function of redshift, and of |RRM| as a function of degree of polarization. The exploration of these quantities can give us clues about the mechanisms that cause depolarization at different frequencies. As a statistical

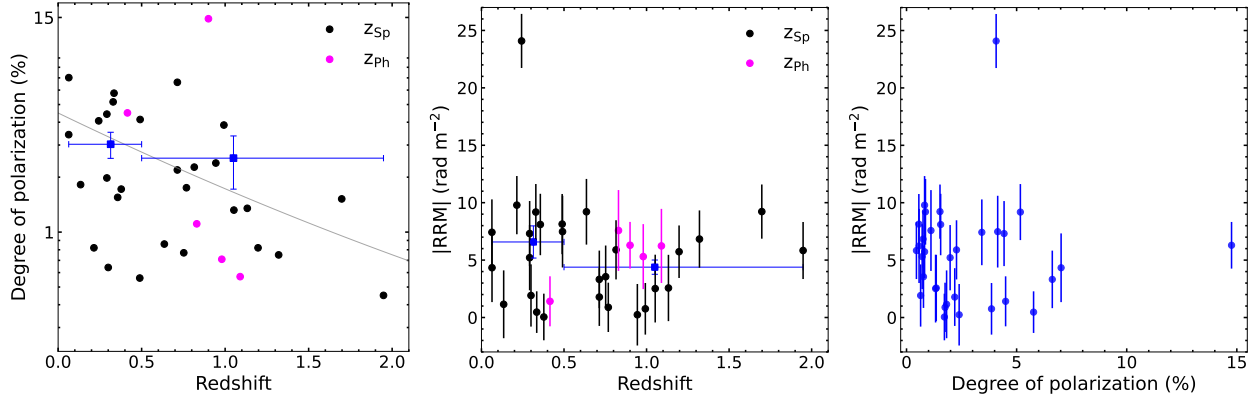


Fig. 6. Variations of degrees of polarization, RRM and redshift values. *Left and middle panels:* degree of polarization and $|RRM|$ as a function of redshift. The sample was split to have a roughly equal number of sources in each redshift bin. Data points from sources with spectroscopic or photometric redshifts are indicated in different colors, as indicated in the legend. The horizontal bars indicate the sizes of the redshift bins, and the vertical bars show the standard errors of the values in the vertical axis. For each plot, the blue squares represent the means of the values in each bin. In the left panel, the gray line is the fit from Carretti et al. (2022) to corresponding data from the LoTSS-DR2 RM grid catalog. *Right panel:* $|RRM|$ vs. degree of polarization.

Table 5. Spearman correlation coefficients and p values for the sample of polarized components in the LOFAR ELAIS-N1 Deep Field.

	Spearman coefficient	p -value
Π vs. z	-0.24	0.19
RRM vs. z	-0.09	0.60
RRM vs. Π	+0.02	0.89

Notes. Π is the degree of polarization.

indicator of a possible correlation, we used the Spearman rank correlation coefficient (a value close to zero indicates no correlation; a value close to +1 indicates a correlation, and -1 indicates an anticorrelation). We also used the probability (p) value, which gives the probability that the null hypothesis (the absence of a correlation between the two considered variables) is correct and that an observed correlation is due to chance. The lower the p value, the higher the probability that the correlation is real. The numbers are given in Table 5.

3.1.1. Degree of polarization versus redshift

Of the three combinations of variables that we considered, the combination with the strongest Spearman correlation coefficient and lowest p value is between the degree of polarization and redshift. These numbers indicate a weak anticorrelation. In the left panel of Fig. 6, we show the fit obtained by Carretti et al. (2022) for the LoTSS-DR2 RM catalog in addition to the values for the 31 polarized components in ELAIS-N1. The anticorrelation in their catalog is stronger. Berger et al. (2021) also reported a decrease in the degree of polarization with increasing redshift in their 1.4 GHz observations of the Lockman Hole.

3.1.2. RRM versus redshift

Studying the NVSS RM catalog, (Hammond et al. 2012) found no significant evolution of the RRM with redshift. At 144 MHz, Carretti et al. (2022) reported no variation in the RRM with redshift either. The central panel of Figure 6 shows the absolute values of the RRM as a function of redshift. We do not find any sign of a correlation.

3.1.3. RRM versus degree of polarization

Finally, we examined the possible variations in the RRM with the degree of polarization of the polarized components. In the LoTSS-DR2 RM sample, the RRM appears to be independent of the degree of polarization, which contradicts the findings at 1.4 GHz of Hammond et al. (2012), who reported a strong anticorrelation between the RRM and the degree of polarization in the NVSS RM data. Carretti et al. (2022) attributed this discrepancy to the different astrophysical origins of the RRM: depolarization at 1.4 GHz would primarily stem from the environment of the local source, while at 144 MHz, it would predominantly be the result of radiation traveling through the intergalactic medium on large scales.

The right panel of Fig. 6 shows the absolute RRM values as a function of the degree of polarization in the ELAIS-N1 Deep Field; these quantities seem to be independent, in agreement with the findings of O’Sullivan et al. (2023) and Carretti et al. (2022).

3.2. Polarized sources in relation to the large-scale structure

The investigation of the extragalactic environment offers information about the magneto-ionic media that interact with the polarized radiation. There is observational evidence for the presence of magnetic fields within galaxy clusters (e.g., Govoni & Feretti 2004; Clarke 2004) and intergalactic filaments (e.g., O’Sullivan et al. 2019). Polarized radio sources in the background of clusters or in the clusters themselves may provide information on intracluster magnetic fields in the cluster that causes the Faraday effect. At 1.4 GHz, Bonafede et al. (2011) and Osinga et al. (2022) found that the fractional polarization of background sources decreases toward the cluster center. Stuardi et al. (2020) studied the intergalactic magnetic fields along the lines of sight of giant radio galaxies detected in the LoTSS-DR2 and showed that the detection of polarized sources is disfavored by the presence of foreground galaxy clusters. They found that the higher RM variance due to turbulence in a foreground intracluster medium influences the fractional polarization at gigahertz frequencies and depolarizes the radio emission at 144 MHz below the detection limit of LoTSS. Furthermore, they suggested that the background polarized sources can be detected probably

Table 6. Nearby superclusters in the field and their cluster members.

Source	RRM (rad m ⁻²)	z_{source}	Supercluster	$z_{\text{supercluster}}$	Cluster	RA, Dec, z_{cluster} (deg, deg)
(1)	(2)	(3)	(4)	(5)	(6)	(7)
08	$+5.73 \pm 2.26$	1.1215	MSCC 476 ^(a) , SCL 162	0.065	A2168	243.27, +54.16, 0.064
12	-0.76 ± 2.23	0.9928			A2149A	240.35, +53.87, 0.0657
			MSCC 473 ^(b)	0.141	A2149E	240.35, +53.87, 0.139
					A2149F	240.35, +53.87, 0.142

Notes. (4) MSCC is the Main SuperCluster Catalog of [Chow-Martínez et al. \(2014\)](#). SCL: supercluster in the [Einasto et al. 2001](#) catalog. (6) A2149 consists of several components along the same line of sight, so that the coordinates of the components are the same as those of A2149. (7) The redshifts of the clusters are from [Chow-Martínez et al. \(2014\)](#). ^(a)Supercluster with J2000 coordinates RA = 241.84°, Dec = 54.01°. This position corresponds to the geometrical center between the two members of the supercluster, A2168 and A2149A. The three-dimensional separation between the two clusters in the supercluster is $10.8 h_{70}^{-1}$ Mpc ([Chow-Martínez et al. 2014](#)). ^(b)Supercluster with J2000 coordinates RA = 240.35°, Dec = 53.87°. The two clusters in this supercluster are in the same position on the sky, and their line-of-sight separation is $12 h_{70}^{-1}$ Mpc ([Chow-Martínez et al. 2014](#)).

only under particular conditions, for example, when the foreground cluster is poor and/or the polarized emission originates in a very compact region.

We compared the positions of our polarized sources with those of the 1.58 million clusters of galaxies cataloged by [Wen & Han \(2024\)](#), who estimated photometric redshifts and collected available spectroscopic redshifts of galaxies up to $z \sim 1.5$. We also compared the positions of our polarized sources with the sample of galaxy clusters from [Zou et al. \(2022\)](#), who estimated photometric redshifts for galaxies up to $z \sim 1$. Within 25 deg² of ELAIS-N1 lie 1186 galaxy clusters from the catalog of [Wen & Han \(2024\)](#), and 548 from the catalog of [Zou et al. \(2022\)](#). The two catalogs have 125 galaxy clusters in common.

Figure 7 shows the locations of the polarized sources (as crosses) and of the galaxy clusters (as shaded circles). The radius of each circle corresponds to r_{200} , the radius within which the mean density of a cluster is 200 times the critical density of the Universe at the cluster’s redshift, and which approximately represents the outer boundary of a galaxy cluster. The catalogs provide r_{500} values (in Mpc) for each galaxy cluster, and we converted this into angular sizes using the cosmological parameters adopted by the authors⁸. We estimated r_{200} using the relation $r_{500}/r_{200} = 0.7$ ([Ettori & Balestra 2009](#)).

We also show in Fig. 7 the locations of the two nearby superclusters in the field that were identified by [Chow-Martínez et al. \(2014\)](#), who studied superclusters of the Abell/ACO galaxy clusters out to redshift 0.15. The properties of these structures are summarized in Table 6. For each supercluster, [Chow-Martínez et al. \(2014\)](#) gave the value d_{max} , which is the maximum projected distance (in Mpc) between the two member clusters of a supercluster farthest from each other, as a rough indicator of the size of a supercluster. We converted these values into angular sizes using the values that they used for the cosmological parameters (given in footnote 8).

We noted that none of the supercluster members are listed in the cluster catalogs of [Wen & Han \(2024\)](#) or [Zou et al. \(2022\)](#) at the redshift indicated by [Chow-Martínez et al. \(2014\)](#), and that cluster sizes were not provided by the latter. Therefore, we indicate their positions in Fig. 7, but their sizes are arbitrary

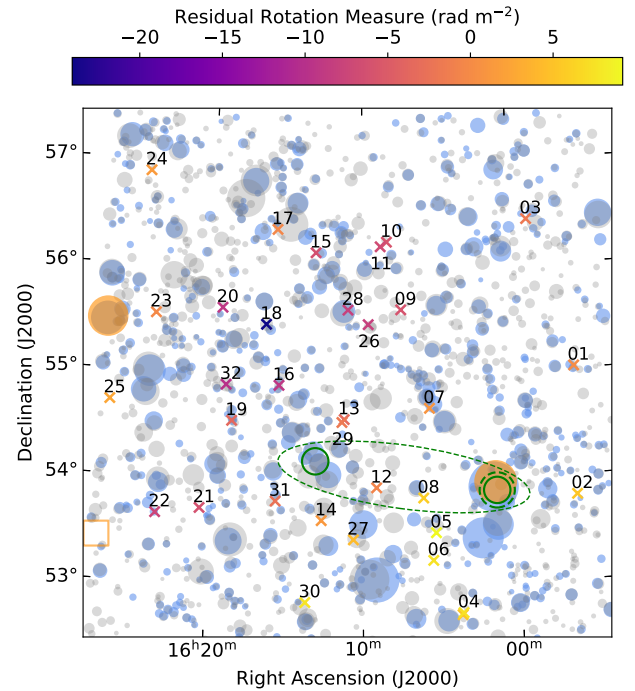


Fig. 7. Galaxy clusters (shaded circles), superclusters, and polarized sources (crosses, with their RRM values as indicated in the color bar) in the ELAIS-N1 LOFAR Deep Field. The radii of the circles indicate r_{200} of the clusters, except for the clusters that are located in superclusters, whose sizes are not known; we used an arbitrary diameter of 30' for the plot (solid green circles). The shaded gray circles represent the clusters of [Wen & Han \(2024\)](#) and the shaded blue circles show the clusters from [Zou et al. \(2022\)](#). The dashed green ellipse and the circle represent the two superclusters from [Chow-Martínez et al. \(2014\)](#) in the field (Table 6). The shaded orange circles represent the clusters detected in X-rays from [Böhringer et al. \(2000\)](#) and/or the PSZ2 [Planck Collaboration XXVII \(2016\)](#) catalogs. The orange square represents the X-ray Sunyaev-Zel'dovich cluster candidate from [Tarrío et al. \(2019\)](#), for which no radius is available.

(30' diameter). Two of our polarized components are positioned behind the supercluster MSCC 476 (sources 8 and 12).

The two superclusters from [Chow-Martínez et al. \(2014\)](#) correspond to pairs of clusters, where one pair is a redshift most component along the line of sight of Abell 2149 (the westernmost of

⁸ [Wen & Han \(2024\)](#), [Zou et al. \(2022\)](#), and [Chow-Martínez et al. \(2014\)](#) adopted the same values for the cosmological parameters, $H_0 = 70 \text{ km s}^{-1} \text{ Mpc}^{-1}$, $\Omega_m = 0.3$, and $\Omega_\Lambda = 0.7$.

Table 7. Polarized sources in the ELAIS-N1 LOFAR Deep Field that might be located behind or are embedded within the galaxy clusters identified by Zou et al. 2022 (Clustering by Fast Search and Find of Density Peaks; CFSFDP) and/or Wen & Han 2024 (WH).

Source	Source redshift	Cluster	Cluster redshift	$R_{200}^{(a)}$ (Mpc)	$\theta_{\text{sep}}^{(b)}$ (arcsec)	$d_{\text{sep}}^{(c)}$ (Mpc)
07	0.7683	CFSFDP 464000084	0.2440	1.14	196	0.75
10	1.9482	WH J160827.0+561505	0.5396	0.78	85	0.54
16*	0.32936	WH J161531.1+545230	0.3294	0.72	10	0.05
18*	0.24297	WH J161623.7+552702	0.2430	0.85	0	0
19	0.7523	WH J161832.0+543337	0.3918	0.88	94	0.50
		WH J161820.9+543040	0.7944	1.09	136	1.02
22	0.4910	CFSFDP 483700074	0.4672	0.84	27	0.16
26*	0.3566	WH J160929.8+552542	0.2602	0.87	108	0.43
		WH J160919.5+552549	0.3572	0.74	169	0.85
28	0.48882	CFSFDP 445000147	0.2234	1.40	146	0.52
32*	0.21431	WH J161858.7+545228	0.2139	0.86	1	0.003

Notes. Sources with an asterisk are in a cluster. Three of these (sources 16, 18, and 32) are associated with radio galaxies whose host galaxy is the brightest cluster galaxy. ^(a) $R_{200} = R_{500}/0.7$, calculated from the R_{500} values given by the authors in their adopted cosmology (footnote 8). ^(b)Angular separation between the polarized source and the cluster center. ^(c)Projected linear separation between the polarized source and the cluster center.

the green circles in Fig. 7). Supercluster catalogs are very sensitive to the linking length that is used, and the physical reality of these superclusters is doubtful especially for very low numbers of member clusters in a supercluster (e.g., only two for both superclusters discussed here). Sankhyayan et al. (2023) published a catalog of SDSS superclusters using the cluster catalog of Wen & Han (2015). This supercluster catalog does not contain the MSCC clusters 473 and 476 from Chow-Martínez et al. (2014). It does not contain any supercluster in the ELAIS-N1 region. This does not mean that there are none, but that it has been very difficult to identify these structures. The very recent cluster catalogs of Zou et al. (2022), Wen & Han (2024), and Yantovski-Barth et al. (2024) could be used to produce a new large supercluster catalog, but this is beyond the scope of this paper.

In Table 7 we list the nine polarized components that are located along the lines of sight of clusters and whose redshifts are higher than or comparable to those of these clusters. The field also contains galaxy clusters detected in the X-ray and/or through the Sunyaev-Zel'dovich effect (Planck Collaboration XXVII 2016; Tarrío et al. 2019; Böhringer et al. 2000), but none of them is positioned along the line of sight of the detected polarized sources.

To search for a possible excess in RRM due to interaction of radiation from polarized sources with the foreground large-scale structure, we computed the mean absolute value of RRM of the sample of polarized components located in a cluster and/or behind a cluster or a supercluster (11 components: the 9 components in Table 7, and the 2 components in Table 6) in comparison to the value of polarized sources that are not along the line of sight of any structure (22 components). We used the standard error (σ) as a representation of the uncertainty on the values. We found $8.6 \pm 2.0 \text{ rad m}^{-2}$ and 4.4 ± 0.6 , respectively, which agree within 2σ . This suggests that the magnetic fields at that position of the clusters are relatively weak and have a low plasma density. Polarized radiation from background sources that pass through regions of the clusters with a high plasma density and strong magnetic fields, such as the cluster centers, may undergo depolarization due to the high RM dispersion (e.g., Osinga et al. 2022) and be completely depolarized at LOFAR frequencies and sensitivities. Similar findings were reached at

1.4 GHz in the XXL-South field by Eyles et al. (2020), who also detected polarized sources at the edge of the clusters, as defined by their r_{200} values.

Our sample contains four sources that are embedded within clusters (Table 7). In one case (source 32), the distorted morphology of the radio galaxy is indeed suggestive of an interaction of the radio plume with a surrounding intracluster medium.

The absolute RRM values of the sources behind the supercluster agree within 2σ with the mean absolute value of the sources that are not located behind any structure. Again, this may indicate very weak magnetic fields and low-density plasma at these positions of the supercluster. A larger sample is needed to measure an effect.

4. Conclusions

We characterized the polarization properties of 31 submillijansky extragalactic sources observed in the ELAIS-N1 LOFAR Deep Field that were originally presented in Paper I. The work is based on the most sensitive polarization data acquired at 146 MHz to date. Our analysis revealed that the morphological features of nearly half of the sources are consistent with FR II radio galaxies, and the remaining half is divided among FR I-type radio galaxies, compact sources, and diffuse sources. Notably, similarly to the LoTSS-DR2 RM catalog of O'Sullivan et al. (2020), the submillijansky-polarized sources tend to be large radio galaxies. Our deeper observations enabled the detection of fainter sources that are more distant and/or intrinsically less luminous sources, as expected.

We produced a residual rotation measure map of the ELAIS-N1 region. The median RRM value is close to zero, as in the LoTSS-DR2 RM. This is an indication that the Galactic RM inferred by Hutschenreuter et al. (2022) was a reasonable estimate, and it suggests that the polarization angle experiences a random walk through the intervening intergalactic magnetized medium. However, some of the overall gradient seen the GRM map remains in the RRM map, which may be a sign of residual GRM contamination. Future deep polarization surveys such as those planned with the Square Kilometre Array will enable the construction of denser RM grids and improved GRM/RRM separations.

Furthermore, we found that the RRM values at 146 MHz remain independent of the degrees of polarization for submilli-jansky sources, which further supports the notion that the RRM at these frequencies is dominated by contributions from the intergalactic medium and not by the local medium. By plotting degrees of polarization versus projected distance of the polarized components to the centers of the host galaxies for the LoTSS-DR RM catalog, we found an increase beyond 100 kpc, which indicates that the local medium contributes to the depolarization.

When we compared our source population to the known locations of clusters and superclusters from the existing literature, we observed that the depolarization and RM properties of sources toward clusters and superclusters are similar to those observed in the entire source population. Consequently, it appears that these structures contribute very little to these properties.

Our work highlights the need for deeper surveys to reveal previously undetected populations of polarized extragalactic sources and to fully characterize their properties to understand the cosmic magnetic field structure.

Data availability

The full catalog of properties of detected polarized sources and references are available in electronic form at the CDS via anonymous ftp to cdsarc.cds.unistra.fr (130.79.128.5) or via <https://cdsarc.cds.unistra.fr/viz-bin/cat/J/A+A/693/A100>.

Appendix B is available at the link <https://zenodo.org/records/14012234>.

Acknowledgements. We are very grateful to the referee, Heinz Andernach, for a constructive and thorough report that led to a significant improvement of the paper. LOFAR, the Low Frequency Array designed and constructed by ASTRON, has facilities in several countries, that are owned by various parties (each with their own funding sources), and that are collectively operated by the International LOFAR Telescope (ILT) foundation under a joint scientific policy. This work was done within the LOFAR Surveys and the LOFAR Magnetism Key Science Projects. This research has made use of the NASA/IPAC Extragalactic Database (NED) which is operated by the Jet Propulsion Laboratory, California Institute of Technology, under contract with the National Aeronautics and Space Administration. This research has made use of the Vizier catalog access tool, CDS, Strasbourg, France. The original description of the Vizier service was published in A&AS 143, 23. We have also made use of the table analysis software *topcat* (Taylor 2005). This research made use of *Astropy*, a community-developed core Python package for astronomy (Astropy Collaboration 2013), of *Matplotlib* (Hunter 2007), and of *APLpy* (Robitaille & Bressert 2012), an open-source astronomical plotting package for Python. This research has made use of the CIRADA cutout service at URL cutouts.cirada.ca, operated by the Canadian Initiative for Radio Astronomy Data Analysis (CIRADA). CIRADA is funded by a grant from the Canada Foundation for Innovation 2017 Innovation Fund (Project 35999), as well as by the Provinces of Ontario, British Columbia, Alberta, Manitoba and Quebec, in collaboration with the National Research Council of Canada, the US National Radio Astronomy Observatory and Australia's Commonwealth Scientific and Industrial Research Organisation. The processing of LOFAR data was enabled by resources provided by the Swedish National Infrastructure for Computing (SNIC) at Chalmers Centre for Computational Science and Engineering (C3SE) partially funded by the Swedish Research Council through grant agreement no. 2018-05973. S.P.O. acknowledges support from the Comunidad de Madrid Atracción de Talento program via grant 2022-T1/TIC-23797. V.V. acknowledges support from the Premio per Giovani Ricercatori “Gianni Tofani” II edizione, promoted by INAF-Osservatorio Astrofisico di Arcetri (DD n. 84/2023). I.P. acknowledges support from INAF under the Large Grant 2022 funding scheme (project “MeerKAT and LOFAR Team up: a Unique Radio Window on Galaxy/AGN co-Evolution”).

References

- Ahn, C. P., Alexandroff, R., Allende Prieto, C., et al. 2012, *ApJS*, **203**, 21
Ahumada, R., Allende Prieto, C., Almeida, A., et al. 2020, *ApJS*, **249**, 3
An, F., Vaccari, M., Best, P. N., et al. 2024, *MNRAS*, **528**, 5346
Astropy Collaboration (Robitaille, T. P., et al.) 2013, *A&A*, **558**, A33
Berger, A., Adebahr, B., Herrera Ruiz, N., et al. 2021, *A&A*, **653**, A155
Böhringer, H., Voges, W., Huchra, J. P., et al. 2000, *ApJS*, **129**, 435
Bonafede, A., Govoni, F., Feretti, L., et al. 2011, *A&A*, **530**, A24
Carretti, E., Vacca, V., O’Sullivan, S. P., et al. 2022, *MNRAS*, **512**, 945
Carretti, E., O’Sullivan, S. P., Vacca, V., et al. 2023, *MNRAS*, **518**, 2273
Chow-Martínez, M., Andernach, H., Caretta, C. A., & Trejo-Alonso, J. J. 2014, *MNRAS*, **445**, 4073
Clarke, T. E. 2004, *J Korean Astron. Soc.*, **37**, 337
Condon, J. J., & Matthews, A. M. 2018, *PASP*, **130**, 073001
Condon, J. J., Cotton, W. D., Greisen, E. W., et al. 1998, *AJ*, **115**, 1693
DESI Collaboration (Adame, A. G., et al.) 2024, *AJ*, **168**, 58
Duncan, K. J., Kondapally, R., Brown, M. J. I., et al. 2021, *A&A*, **648**, A4
Einasto, M., Einasto, J., Tago, E., Müller, V., & Andernach, H. 2001, *AJ*, **122**, 2222
Ettori, S., & Balestra, I. 2009, *A&A*, **496**, 343
Eyles, R. A. J., Birkinshaw, M., Smolčić, V., et al. 2020, *A&A*, **633**, A6
Falco, E. E., Kochanek, C. S., & Muñoz, J. A. 1998, *ApJ*, **494**, 47
Fanaroff, B. L., & Riley, J. M. 1974, *MNRAS*, **167**, 31P
Govoni, F., & Feretti, L. 2004, *Int. J. Mod. Phys. D*, **13**, 1549
Grant, J. K., Taylor, A. R., Stil, J. M., et al. 2010, *ApJ*, **714**, 1689
Hammond, A. M., Robishaw, T., & Gaensler, B. M. 2012, arXiv e-prints [arXiv:1209.1438]
Herrera Ruiz, N., O’Sullivan, S. P., Vacca, V., et al. 2021, *A&A*, **648**, A12
Hunter, J. D. 2007, *Comput. Sci. Eng.*, **9**, 90
Hutschenreuter, S., Anderson, C. S., Betti, S., et al. 2022, *A&A*, **657**, A43
Kondapally, R., Best, P. N., Hardcastle, M. J., et al. 2021, *A&A*, **648**, A3
Lacy, M., Baum, S. A., Chandler, C. J., et al. 2020, *PASP*, **132**, 035001
Mahatma, V. H., Hardcastle, M. J., Harwood, J., et al. 2021, *MNRAS*, **502**, 273
Mandal, S., Prandoni, I., Hardcastle, M. J., et al. 2021, *A&A*, **648**, A5
Massaro, E., Maselli, A., Leto, C., et al. 2015, *Ap&SS*, **357**, 75
Mingo, B., Croston, J. H., Hardcastle, M. J., et al. 2019, *MNRAS*, **488**, 2701
Mingo, B., Croston, J. H., Best, P. N., et al. 2022, *MNRAS*, **511**, 3250
Osinga, E., van Weeren, R. J., Boxelaar, J. M., et al. 2021, *A&A*, **648**, A11
Osinga, E., van Weeren, R. J., Andrade-Santos, F., et al. 2022, *A&A*, **665**, A71
O’Sullivan, S. P., Machalski, J., Van Eck, C. L., et al. 2019, *A&A*, **622**, A16
O’Sullivan, S. P., Brüggem, M., Vazza, F., et al. 2020, *MNRAS*, **495**, 2607
O’Sullivan, S. P., Shimwell, T. W., Hardcastle, M. J., et al. 2023, *MNRAS*, **519**, 5723
Piras, S., Horellou, C., Conway, J. E., et al. 2024, *A&A*, **687**, A267
Planck Collaboration XIII. 2016, *A&A*, **594**, A13
Planck Collaboration XXVII. 2016, *A&A*, **594**, A27
Richards, G. T., Myers, A. D., Gray, A. G., et al. 2009, *ApJS*, **180**, 67
Robitaille, T., & Bressert, E. 2012, *Astrophysics Source Code Library* [record ascl:1208.017]
Sabater, J., Best, P. N., Tasse, C., et al. 2021, *A&A*, **648**, A2
Sankhyayan, S., Bagchi, J., Tempel, E., et al. 2023, *ApJ*, **958**, 62
Shimwell, T. W., Röttgering, H. J. A., Best, P. N., et al. 2017, *A&A*, **598**, A104
Shimwell, T. W., Tasse, C., Hardcastle, M. J., et al. 2019, *A&A*, **622**, A1
Shimwell, T. W., Hardcastle, M. J., Tasse, C., et al. 2022, *A&A*, **659**, A1
Simonte, M., Andernach, H., Brüggem, M., Best, P. N., & Osinga, E. 2023, *A&A*, **672**, A178
Simonte, M., Andernach, H., Brüggem, M., Miley, G. K., & Barthel, P. 2024, *A&A*, **686**, A21
Šnidarić, I., Jelić, V., Mevius, M., et al. 2023, *A&A*, **674**, A119
Stuardi, C., O’Sullivan, S. P., Bonafede, A., et al. 2020, *A&A*, **638**, A48
Tarrío, P., Melin, J. B., & Arnaud, M. 2019, *A&A*, **626**, A7
Taylor, M. B. 2005, *ASP Conf. Ser.*, **347**, 29
Taylor, A. R., Stil, J. M., & Sunstrum, C. 2009, *ApJ*, **702**, 1230
Van Eck, C. L., Haverkorn, M., Alves, M. I. R., et al. 2018, *A&A*, **613**, A58
Vernstrom, T., Gaensler, B. M., Rudnick, L., & Andernach, H. 2019, *ApJ*, **878**, 92
Wen, Z. L., & Han, J. L. 2015, *ApJ*, **807**, 178
Wen, Z. L., & Han, J. L. 2024, *ApJS*, **272**, 39
Yantovski-Barth, M. J., Newman, J. A., Dey, B., et al. 2024, *MNRAS*, **531**, 2285
Zou, H., Sui, J., Xue, S., et al. 2022, *Res. Astron. Astrophys.*, **22**, 065001

Appendix A: Properties of detected polarized sources

Table A.1: Catalog of properties of polarized sources in the ELAIS-N1 LOFAR deep field.

Source	RM (rad m^{-2}) (2)	GRM (rad m^{-2}) (3)	RRM (rad m^{-2}) (4)	Angular size (arcsec) (5)	Linear size (kpc) (6)	Flux (mJy) (7)	$\log_{10}(\text{Luminosity})$ (8)	Redshift (9)	Redshift type (10)	Host classification (11)	Radio morphology (12)
(1)											
01	1.68 ± 0.02	1.63 ± 2.01	0.05 ± 2.01	17	91	163	25.89	0.37779	s	QSO	FRII
02 ^(*)	9.71 ± 0.05	4.41 ± 2.78	5.30 ± 2.78	35	285	471	27.30	0.98	p	QSO	FRII
03	-5.83 ± 0.02	-3.91 ± 2.69	-1.92 ± 2.69	10	45	602	26.23	0.3	s	BI	OE
04 _A	19.68 ± 0.01	14.47 ± 2.83	5.21 ± 2.83	77	349	1737	26.66	0.29186	s	QSO	FRII
04 _B	21.78 ± 0.01	14.47 ± 2.83	7.31 ± 2.83	77	349	1737	26.66	0.29186	s	QSO	FRII
05	19.12 ± 0.05	9.91 ± 2.81	9.21 ± 2.81	33	233	196	26.49	0.6359	s	G	FRII
06	18.43 ± 0.03	11.01 ± 2.84	7.42 ± 2.84	300	378	209	24.32	0.06333	s	G	FRI
07	6.062 ± 0.003	5.17 ± 2.15	0.89 ± 2.15	12	91	1299	27.51	0.7683	s	G	FRII
08	13.39 ± 0.03	7.66 ± 2.26	5.73 ± 2.26	61	521	338	27.36	1.197	s	G	FRII
09	-3.79 ± 0.03	2.10 ± 2.55	-5.89 ± 2.55	1	9	24	25.82	0.81512	s	G	C
10	-5.61 ± 0.05	0.22 ± 2.43	-5.83 ± 2.43	3	27	122	27.40	1.94822	s	BI	C
11	-6.24 ± 0.04	0.59 ± 2.45	-6.83 ± 2.45	152	1308	511	27.63	1.32046	s	QSO	FRII
12	7.17 ± 0.02	7.93 ± 2.23	-0.76 ± 2.23	142	1169	458	27.30	0.99258	s	QSO	FRII
13 _A	2.38 ± 0.04	5.70 ± 2.47	-3.32 ± 2.47	129	956	41	25.92	0.71385	s	QSO	FRII
14	10.31 ± 0.02	9.16 ± 2.93	1.15 ± 2.93	53	130	122	24.78	0.13455	s	G	FRI
15 ^(*)	-4.80 ± 0.04	1.49 ± 1.99	-6.29 ± 1.99	96	769	70	26.38	0.9	p	G	FRII
16	-4.01 ± 0.05	5.17 ± 2.39	-9.18 ± 2.39	45	220	74	25.41	0.32936	s	G	OE
17	1.95 ± 0.03	2.42 ± 1.78	-0.47 ± 1.78	64	315	118	25.63	0.3347	s	G	FRII
18	-20.31 ± 0.03	3.78 ± 2.33	-24.09 ± 2.33	144	569	167	25.48	0.24297	s	G	FRI
19	2.91 ± 0.04	6.46 ± 2.68	-3.55 ± 2.68	30	227	260	26.78	0.7523	s	G	FRII
20	-4.70 ± 0.02	4.52 ± 2.34	-9.22 ± 2.34	36	313	144	27.34	1.6981	s	BI	OE
21 ^(*)	3.29 ± 0.04	9.52 ± 3.19	-6.23 ± 3.19	27	226	348	27.28	1.09	p	G	FRII
22	2.31 ± 0.05	9.79 ± 3.07	-7.48 ± 3.07	15	93	93	25.90	0.491	s	G	OE
23	5.91 ± 0.05	6.15 ± 2.63	-0.24 ± 2.63	257	2089	67	26.41	0.9443	s	G	FRII
24	9.43 ± 0.01	8.02 ± 2.17	1.41 ± 2.17	6	34	258	26.18	0.415	p	BI	C
25	10.03 ± 0.02	7.46 ± 2.87	2.57 ± 2.87	6	53	135	26.91	1.1326	s	QSO	C
26	-5.38 ± 0.07	2.72 ± 2.60	-8.10 ± 2.61	158	817	215	25.95	0.3566	s	QSO	FRII
27	14.17 ± 0.07	9.84 ± 2.92	4.33 ± 2.92	111	141	190	24.30	0.06389	s	G	FRII
28	-5.74 ± 0.05	2.40 ± 2.57	-8.14 ± 2.57	8	51	68	25.76	0.48882	s	G	OE
29 (13 _B)	3.92 ± 0.05	5.70 ± 2.47	-1.78 ± 2.47	129	956	41	25.92	0.71385	s	QSO	FRII
30 ^(*)	19.40 ± 0.07	11.82 ± 3.45	7.58 ± 3.45	30	758	207	26.78	0.83	p	G	FRII
31	6.23 ± 0.06	8.75 ± 2.89	-2.52 ± 2.89	38	315	328	27.23	1.0524	s	G	FRII
32	-4.05 ± 0.06	5.74 ± 2.48	-9.79 ± 2.48	140	504	116	25.20	0.21431	s	G	FRI

(1) Name of polarized source, as in Paper I; Source 04_A and 04_B are two lobes of the same radio galaxy; Source 13_A and 29 (or 13_B) are two lobes of the same radio galaxy; (2) RM and RM error of polarized source, from Paper I; (3) GRM and GRM error at the location of the polarized sources; (4) RRM and RRM error at the location of the polarized sources; (5) angular size of radio galaxy, including components undetected in polarization; (6) projected linear size of radio galaxy, including components undetected in polarization; (7) flux density in Stokes I integrated over the radio source; (8) logarithm of rest-frame luminosity in W Hz^{-1} at 146 MHz; (9) redshift of host galaxy; (10) redshift type, p = photometric redshift, s = spectroscopic redshift; (11) Host classification, QSO = Quasi-Stellar Object, BI = blazar, G = galaxy;

(12) Radio morphology classification at 146 MHz, C = compact, OE = other extended, FRI = FRI radio galaxy, FRII = FRII radio galaxy.

^(*) The photometric redshifts of these sources are from Simonte et al. (2024), who determined them by averaging the photometric redshifts from multiple catalogs. The full Table and references are available at the CDS.

Appendix B: Images and Faraday spectra

The Stokes I images from Sabater et al. (2021) are shown in contours and the polarized intensity in blue colors. The contours increase by factors of $\sqrt{2}$ and start at 100 times the noise level of the Stokes I map, $\sigma_I = 30 \mu\text{Jy beam}^{-1}$ for sources 02, 03, 04, 05, 07, 08, 09, 10, 19, 24, and 30; start at $50\sigma_I$ for sources 01, 11, 17, 21, 22, 25, 28, and 31; start at $20\sigma_I$ for sources 12, 15, 20, 26, and 32; start at $5\sigma_I$ for source 23; start at $10\sigma_I$ for the remaining sources. The red crosses indicate the locations of the host galaxies. The orange square indicate the locations of the detections from Grant et al. (2010). The Faraday spectra correspond to the locations of the polarized intensity peaks. The instrumental region near 0 rad m^{-2} is shaded in gray. The horizontal red lines show the $8\sigma_{\text{QU}}$ and $6\sigma_{\text{QU}}$ thresholds according to Paper I. In the upper left of each contour map are the source number and the redshift of the source.

Appendix C: Description of the sources

Each detected polarized source was visually inspected in the 6-arcsecond-resolution LOFAR Stokes I image from Sabater et al. (2021) to assess its morphology. We also inspected Quick Look images from the VLASS taken in different epochs (VLASS 1.1, VLASS 2.1, VLASS 3.1; 2–4 GHz band, 2.5 arcsec-resolution; Lacy et al. 2020). The references for the redshifts quoted below are given in Table A and are repeated here only in some special cases.

Source 01 (ILT J155603.98+550056.8) is an FR II radio galaxy in the LOFAR image and in VLASS. We detected polarization from the western lobe. The host galaxy has been classified as a quasar at spectroscopic redshift $z = 0.37779$.

Source 02 (ILT J155614.81+534814.8) is an FR II radio galaxy both in the LOFAR and in the VLASS image. The polarized emission comes from the southern lobe. The host galaxy has been classified as a quasar at photometric redshift $z = 0.98$.

Source 03 (ILT J155848.42+562514.4) is an extended source in the LOFAR image and is compact in VLASS. It is associated with an early-type galaxy with spectroscopic redshift $z = 0.30 \pm 0.03$ measured from detection of three absorption lines (Falco et al. 1998). This is the redshift value that we used. We note that there are conflicting values in the literature: the SDSS spectrum shows no lines, but a spectroscopic redshift of 3.37 is given in the SDSS DR16 catalog (Ahumada et al. 2020), which might be due to misidentification by the pipeline. The Roma BZCAT multiwavelength catalog of blazars quotes $z = 0$ (Massaro et al. 2015). It was detected in polarization with LOFAR by Herrera Ruiz et al. (2021) and the RM values at 150 MHz are consistent within 1σ .

Source 04 (ILT J160344.42+524228.0) is an FR II radio galaxy both in the LOFAR and the VLASS images. We detected polarized emission from both lobes with slightly different RM values: $19.68 \pm 0.01 \text{ rad m}^{-2}$ for source 04_A and $21.78 \pm 0.01 \text{ rad m}^{-2}$ for source 04_B. The RMs agree with the value at 1.4 GHz from the NVSS RM catalog. Between the lobes there is a quasar at spectroscopic redshift $z = 0.29186$.

Source 05 (ILT J160520.16+532837.2) is FR II radio galaxy both in the LOFAR and the VLASS image. The polarized emission comes from the eastern hotspot. The spectroscopic redshift of the host galaxy is $z = 0.6359$.

Source 06 (ILT J160532.84+531257.4) is an FRI radio galaxy at 150 MHz and a compact source at 3 GHz. The polarized emission comes from the nucleus of the radio galaxy. It was detected by Herrera Ruiz et al. (2021) and the RM values at 150 MHz are consistent within 1σ . The associated spectroscopic redshift is $z = 0.06333$.

Source 07 (ILT J160538.33+543922.6), the reference source that we used in the stacking process (Paper I), seems to be an FR II radio galaxy in the LOFAR image, and indeed we see clearly the double-lobed structure in the VLASS image. The polarized emission comes from the south-western component. The peculiarity of this source is a star superposed within $1''$ of the peak of SW hotspot in VLASS, which could be mistaken as the host of one-sided source. The real host (which is marked in Fig. B) is much fainter than the superposed star. The RM is consistent with that found by Herrera Ruiz et al. (2021). The spectroscopic redshift is $z = 0.7683$.

Source 08 (ILT J160603.11+534812.6) was classified as an FR II radio galaxy at 150 MHz (Mingo et al. 2022) and appears as an FR II in the 3 GHz VLASS image as well. We detected polarized emission from the eastern lobe. The spectroscopic redshift of the host galaxy is $z = 1.1970$.

Source 09 (ILT J160725.85+553525.8) is compact in both the LOFAR and the VLASS images. The spectroscopic redshift of the host galaxy is $z = 0.81512$. The Bz

Source 10 (ILT J160820.72+561355.7) is compact both at 150 MHz and 3 GHz. The host galaxy has been classified as a quasar at spectroscopic redshift $z = 1.9482$ from Ahumada et al. (2020). It is classified as a blazar in the Roma BZCAT multiwavelength catalog (Massaro et al. 2015).

Source 11 (ILT J160851.99+561109.3) was classified as an FR II at LOFAR frequencies (Mingo et al. 2022) and resolved as an FR II in the VLASS image, too. We detected polarized emission from the western lobe. The host galaxy has been classified as a quasar at spectroscopic redshift $z = 1.3204$.

Source 12 (ILT J160909.99+535426.8) is an FR II radio galaxy in the LOFAR image, but the eastern lobe is not visible in the VLASS image. We detected polarized emission from the western lobe. Herrera Ruiz et al. (2021) found a RM value of $7.30 \pm 0.02 \text{ rad m}^{-2}$, we found $7.17 \pm 0.02 \text{ rad m}^{-2}$. The host galaxy has been classified as a quasar at spectroscopic redshift $z = 0.99258$ from Ahumada et al. (2020). It is classified as a blazar in the Roma BZCAT multiwavelength catalog (Massaro et al. 2015).

Source 13_A (ILT J161118.03+543218.1) is the northern lobe of an FR II radio galaxy in the LOFAR image (Mingo et al. 2022), but is not detected at 3 GHz. The southern lobe is identified as Source 29 (or 13_B) and is polarized in the $6\text{--}8\sigma_{\text{QU}}$ range. Between the lobes there is a quasar at spectroscopic redshift $z = 0.71385$.

Source 14 (ILT J161240.15+533558.3) is an FRI radio galaxy in the LOFAR image and is a compact source in VLASS. The polarized emission comes from the nucleus of the radio galaxy. The spectroscopic redshift is $z = 0.13455$. This source has also been detected by Herrera Ruiz et al. (2021) and the RM values are consistent within 2σ .

Source 15 (ILT J161314.05+560810.8) appears as an FR II radio galaxy in the LOFAR image and it is not detected in VLASS. The polarized emission is found on the western lobe. Close to the middle between the two lobes the $r = 23.37$ magnitude galaxy

DESI J243.2976+56.1347 had been identified by [Simonte et al. \(2024\)](#) as the host, who give $z_{\text{ph}} = 0.9 \pm 0.1$ and a size of 96 arcsec for the entire source.

Source 16 (ILT J161530.73+545232.4) shows diffuse emission at 150 MHz and is not detected at 3 GHz. The host galaxy has a spectroscopic redshift $z = 0.32936$.

Source 17 (ILT J161548.48+562029.8) is an FR II radio galaxy in the LOFAR image and in VLASS. [Herrera Ruiz et al. \(2021\)](#) measured an RM value of $1.43 \pm 0.04 \text{ rad m}^{-2}$, we found $1.95 \pm 0.03 \text{ rad m}^{-2}$. Polarized emission is detected in the north-western lobe. The spectroscopic redshift is $z = 0.3347$.

Source 18 (ILT J161623.79+552700.8) is an FRI radio galaxy with LOFAR ([Mingo et al. 2022](#)) and it is unresolved in VLASS. The polarized emission is associated with the central component of the radio galaxy. It has been detected also by [Herrera Ruiz et al. \(2021\)](#) with an RM of $-20.15 \pm 0.03 \text{ rad m}^{-2}$; we measured an RM of $-20.31 \pm 0.03 \text{ rad m}^{-2}$ in the 6'' data. The host galaxy has a spectroscopic redshift $z = 0.24297$.

Source 19 (ILT J161832.97+543146.3) is the polarized component associated with the northern hotspot of an FR II radio galaxy. The spectroscopic redshift of the galaxy is $z = 0.7523$.

Source 20 (ILT J161919.70+553556.7) was classified as an FRI radio galaxy by [Mingo et al. 2022](#). However, this source is very core-dominated in the LOFAR image and seems to have a one-sided jet in the SSW direction, of which just the beginning can be recognized in the VLASS images. It is classified as blazar in NED. Calling such a one-sided blazar-like source an FRI may be misleading, so we classified it as "Other Extended" in Table A. The attribution of a redshift is complicated: we used $z = 1.698$ (spectroscopic) from [DESI Collaboration \(2024\)](#), but other values are given in the literature: [Duncan et al. \(2021\)](#) gave $z = 0.701$ (photometric); [Herrera Ruiz et al. \(2021\)](#) cited $z = 0.405$ (photometric) from [Richards et al. \(2009\)](#); [Ahn et al. \(2012\)](#) gave $z = 5.5539$ (spectroscopic).

Source 21 (ILT J162027.55+534208.8) is an FR II radio galaxy in the LOFAR and VLASS images. Polarized emission is detected from the south-eastern lobe. This is a 27'' large asymmetric FR II listed in [Simonte et al. 2024](#) with $z = 1.09 \pm 0.21$ (photometric) from three references, coincident with a faint VLASS radio core close to the north-western hotspot.

Source 22 (ILT J162318.64+533847.4) is an extended radio source at 150 MHz and 3 GHz. This source is associated with an optical galaxy with spectroscopic redshift $z = 0.4910$.

Source 23 (ILT J162027.55+534208.8) is the SW lobe of a 4.3' large FR II listed in [Simonte et al. \(2024\)](#) with $z = 0.9443$ (spectroscopic) from SDSS.

Source 24 (ILT J162432.20+565228.5) is compact both in LOFAR and VLASS images. It was also detected in polarization by [Herrera Ruiz et al. \(2021\)](#) and the RMs found are consistent within 2σ . It is cataloged in NED as a blazar and the photometric redshift is 0.415 ([Richards et al. 2009](#)). It is classified as a blazar also in the Roma BZCAT multiwavelength catalog ([Massaro et al. 2015](#)).

Source 25 (ILT J162634.18+544207.8) is a compact source in LOFAR and in VLASS. It is identified as a quasar, with spectroscopic redshift of $z = 1.1326$.

Source 26 (ILT J160936.45+552659.0) is an FR II radio galaxy at LOFAR frequencies ([Mingo et al. 2022](#)), but is very faint at 3 GHz. We detected polarization from the northern lobe. The host galaxy has been classified as a quasar at spectroscopic redshift $z = 0.3566$.

Source 27 (ILT J161037.49+532425.1) appears as an FR II radio galaxy in the LOFAR image, and is barely visible in VLASS. In [Mingo et al. \(2022\)](#) it is classified as an FRI, but it has very diffuse lobes and could also be a remnant FR II. The luminosity we computed ($\sim 2 \times 10^{24} \text{ W Hz}^{-1}$) is more consistent with an FRI type. However, [Mingo et al. \(2022\)](#) also identified a few FR IIs at similarly low luminosities. The host galaxy has a spectroscopic redshift of $z = 0.06389$.

Source 28 (ILT J161057.72+553527.9) is an extended source both in the LOFAR image and in VLASS. The optical counterpart has a spectroscopic redshift of $z = 0.48882$.

Source 29, or 13_B, (ILT J162347.10+553207.2) coincides with the southern lobe of an FR II radio galaxy at 150 MHz; it is not visible in the VLASS image at 3 GHz. The polarized emission that we detected from that lobe was in the $6 - 8\sigma_{\text{QU}}$ range, while it was detected above $8\sigma_{\text{QU}}$ in the northern lobe.

Source 30 (ILT J161340.99+524913.0) is the north-western lobe of 30''-wide FR II, very symmetric in VLASS, that had also been identified by [Simonte et al. \(2024\)](#) with DESI J243.4211+52.8203, right at the symmetry center, and with $z = 0.83 \pm 0.05$ (photometric) from four different references.

Source 31 (ILT J161537.86+534646.4) is an FR II radio galaxy at 150 MHz and looks like a FR II at 3 GHz. It is classified as an FRI by [Mingo et al. \(2022\)](#). We detected polarization from the central part of the galaxy, which has a spectroscopic redshift of $z = 1.0524$.

Source 32 (ILT J161859.41+545246.3) is an FRI radio galaxy at 150 MHz ([Mingo et al. 2022](#)). At 3 GHz a central component is clearly visible while a lobe is barely detected. We detected polarized emission from the central component. The spectroscopic redshift of the galaxy is $z = 0.21431$. The host galaxy we identified differs from the fainter one (SDSS J161859.62+545246.8) proposed by [Simonte et al. \(2024\)](#), although both are at the same redshift. However, the wide-angle tailed radio morphology suggests that our identified host is the correct one. It is the brightest cluster galaxy WH J161858.7+545228 listed in [Wen & Han \(2024\)](#), as reported in Table 7.